Draft version June 16, 2017
Preprint typeset using LaTeX style emulateapj v. 2/16/10

THERMAL JEANS FRAGMENTATION WITHIN 1000 AU IN OMC-1S

Aina Palau[1], Luis A. Zapata[1], Carlos G. Román-Zúñiga[2], Álvaro Sánchez-Monge[3], Robert Estalella[4], Gemma Busquet[5], Josep M. Girart[5], Asunción Fuente[6], Benoit Commerçon[7]

Draft version June 16, 2017

ABSTRACT

We present subarcsecond 1.3 mm continuum ALMA observations towards the Orion Molecular Cloud 1 South (OMC-1S) region, down to a spatial resolution of $\sim$ 100 AU. The observations reveal a total of 31 continuum sources, which are grouped in cores along three main filaments, with the cores being separated about $\sim$ 2000 AU in the filaments. We also present subarcsecond 7 mm continuum VLA observations of the same region, which allow to further study fragmentation in each core down to a spatial resolution of 40 AU. Typical separations between fragments are $\lesssim$ 560 AU and $\sim$ 2900 AU, suggesting a two-level fragmentation process. In addition, a higher fragmentation level is clearly found towards the southern filament, which is the one enclosing a higher mass (higher density) within 1000 AU per each fragmenting core. This is fully consistent with previous studies of fragmentation at spatial scales one order of magnitude larger, and suggests that fragmentation down to 40 AU seems to be governed by thermal Jeans processes in OMC-1S.

Subject headings: stars: formation — radio continuum: ISM

1. INTRODUCTION

The processes regulating the fragmentation of molecular clouds are still a matter of vigorous discussion and debate. These processes have been studied from an observational point of view at different spatial scales. At large-scales ($\sim$ 1 pc) or clump scales, gravoturbulent fragmentation (or thermal Jeans fragmentation) seems to describe well the observations (e. g., Román-Zúñiga et al. 2009,Takahashi et al. 2013; Walker-Smith et al. 2013; Samal et al. 2015; Kainulainen et al. 2016a; Sharma et al. 2016; Hacar et al. 2017b), although there are cases where the effects of feedback (Busquet et al. 2016), or large-scale collapse (Csengeri et al. 2017) seem to be important as well. The term of 'gravoturbulent fragmentation' refers to the fragmentation that takes place in a turbulent and self-gravitating cloud. In these clouds, turbulence generates high-density regions where the Jeans mass decreases and thus fragmentation is favored (e. g., Padoan & Nordlund 2002; Schmeja et al. 2004; Hopkins 2013; Gong & Ostriker 2015).

At medium-scales ($\sim$ 0.1 pc), fragmentation also seems to be dominated by gravity acting in a turbulent medium (e. g., Teixeira et al. 2016, Kirk et al. 2017). In this respect, Palau et al. (2014, 2015) compile a sample of 19 massive dense cores and study their fragmentation level against different parameters, finding that the fragmentation level seems to be well correlated with the density within the approximate core size of 0.1 pc, a result consistent with thermal Jeans fragmentation. However, there are also works showing that at these scales the mass of the fragments seem to be too high compared to the thermal Jeans mass (e. g., Zhang et al. 2009, 2015; Bontemps et al. 2010; Wang et al. 2011, 2014; Pillai et al. 2011; Lu et al. 2015). This needs to be further investigated with better mass sensitivities (Henshaw et al. 2017) and in relation to the kinematics of the surrounding molecular gas (e. g., Duarte-Cabral et al. 2013).

At even smaller-scales ($\sim$ 0.01 pc or $\sim$ 1000 AU), the 'fragmentation properties' are usually referred to as 'multiplicity properties', and most studies have been carried out towards low-mass star-forming regions. At these scales, new ingredients such as rotational fragmentation (e. g., Chen et al. 2012; Chabrier et al. 2014) or fragmentation of a (pseudo)disk through gravitational instability (e. g., Kratter & Matzner 2006; Tobin et al. 2016; Guszejnov et al. 2017) have been proposed to explain the formation of multiple/binary systems. Thus, it is not clear whether the dominant process regulating fragmentation at these small scales is inherited from large scales (as suggested by some observational works, Lee et al. 2015), or the aforementioned processes start to be important. At these scales, there is a lack of observations about the fragmentation properties in intermediate and high-mass star-forming regions at very early stages, but is quite well stablished that the multiplicity fraction in high-mass main-sequence stars, as well as the number of companions per system, increases with stellar mass (e. g., Chini et al. 2012, Kraus et al. 2017). Thus, studying the fragmentation/multiplicity properties in deeply embedded intermediate/high-mass star forming regions should provide clues for the dominant processes determining fragmentation at these scales.

Here we present a study of the fragmentation properties of a region forming intermediate and low-mass protostars, the Orion Molecular Cloud 1 South (hereafter, OMC-1S). The region lies near the center of the Integral Shaped Filament (Johnstone & Bally 1999), about 1′ to the south of the BN/KL region and $\sim 2'$ to the north-west of the Orion bar. The most recent measurement of the distance has been done by Kounkel

a.palau@crya.unam.mx
[1] Instituto de Radioastronomía y Astrofísica, Universidad Nacional Autónoma de México, P.O. Box 3-72, 58090, Morelia, Michoacán, México
[2] Instituto de Astronomía, Universidad Nacional Autónoma de México, Apartado Postal 106, 22800 Ensenada, Baja California, México
[3] I. Physikalisches Institut der Universität zu Köln, Zülpicher Strasse 77, 50937 Köln, Germany
[4] Departament de Física Quàntica i Astrofísica, Institut de Ciències del Cosmos (ICC), Universitat de Barcelona (IEEC-UB), Martí Franquès 1, 08028 Barcelona, Spain
[5] Institut de Ciències de l'Espai (CSIC-IEEC), Campus UAB – Facultat de Ciències, Torre C5 – parell 2, 08193 Bellaterra, Catalunya, Spain
[6] Observatorio Astronómico Nacional, Apartado Postal 112, 28803 Alcalá de Henares, Madrid, Spain
[7] École Normale Supérieure de Lyon, CRAL, UMR CNRS 5574, Université Lyon I, 46 Allée d'Italie, 69364 Lyon Cedex 07, France

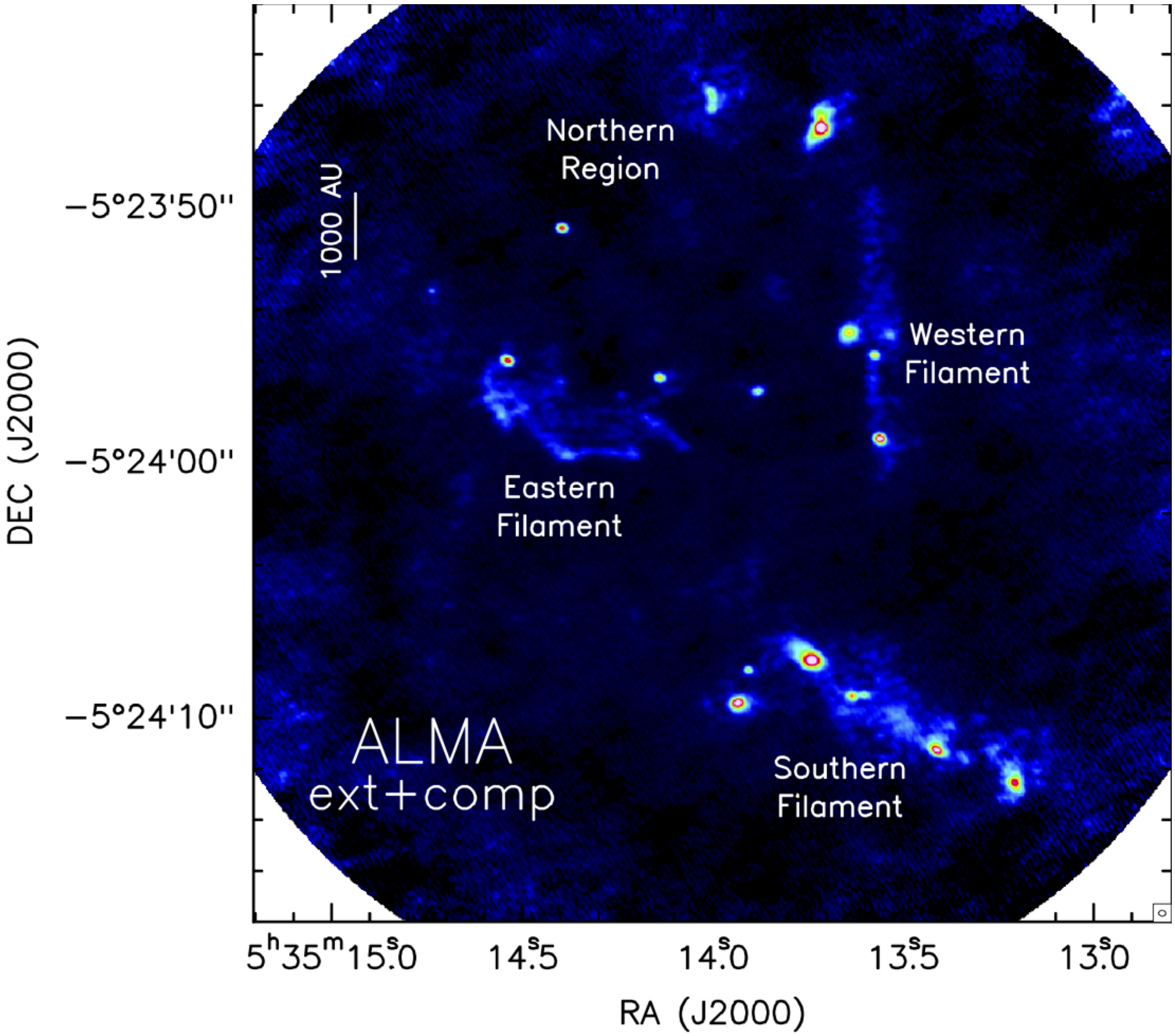

FIG. 1.— ALMA 1.3 mm continuum emission for the OMC-1S region for extended+compact configurations. The ALMA beam, of 0.28″ × 0.22″, is shown in the bottom-right corner; a scale corresponding to 1000 AU is shown in the top-left corner.

et al. (2017), who report 388 pc. OMC-1S has been widely studied using multiple observational techniques, which have revealed a nascent cluster characterized by a large number of spectacular molecular outflows and HH objects (e. g., Smith et al. 2004, Zapata et al. 2005, 2006; Henney et al. 2007). In addition, the outer layers of the OMC-1S region, which are bathed by external irradiation from the surrounding massive stars within the Orion Nebular Cluster (Tahani, Plume & Bergin 2016), also seem to be undergoing global infall (e. g., Hacar et al. 2017a). Therefore, a very active phase of clustered star formation is taking place in OMC-1S, and the region becomes an excellent target to study fragmentation down to very small scales ($\lesssim$ 1000 AU). In Section 2, we present the millimeter ALMA and VLA observations towards OMC-1S down to spatial scales of $\sim$ 40 AU for the VLA observations. In Section 3, we describe the main results. In Section 4, we analyse the properties of the fragmenting cores in OMC-1S; in Section 5 we discuss our main findings, and in Section 6 we give the conclusions.

2. OBSERVATIONS

2.1. *ALMA at 1.3 mm*

The ALMA[8] Band 6 (1.3 mm) observations were carried out on 2015 May 19 and August 18 as part of the Cycle 2 program 2013.1.01037.S. On May 19, we used 38 of the 12 m antennas, yielding baselines with projected lengths from 21 to 555 m (16–427 kλ), while on August 18 we used 37 antennas also of 12 m, yielding baselines with projected lengths from 43 to 1600 m (33–1230 kλ). Including both epochs, the covered range of projected baselines is 16–1230 kλ, which corresponds to a Largest Angular Scale to which ALMA was sensitive of 5.7″ (following equation A5 of Palau et al. 2010). The integration time on-source (OMC-1S) was about 8 minutes in each observation.

[8] ALMA is a partnership of ESO (representing its member states), NSF (USA) and NINS (Japan), together with NRC (Canada) and NSC and ASIAA (Taiwan) and KASI (Republic of Korea), in cooperation with the Republic of Chile. The Joint ALMA Observatory is operated by ESO, AUI/NRAO and NAOJ.

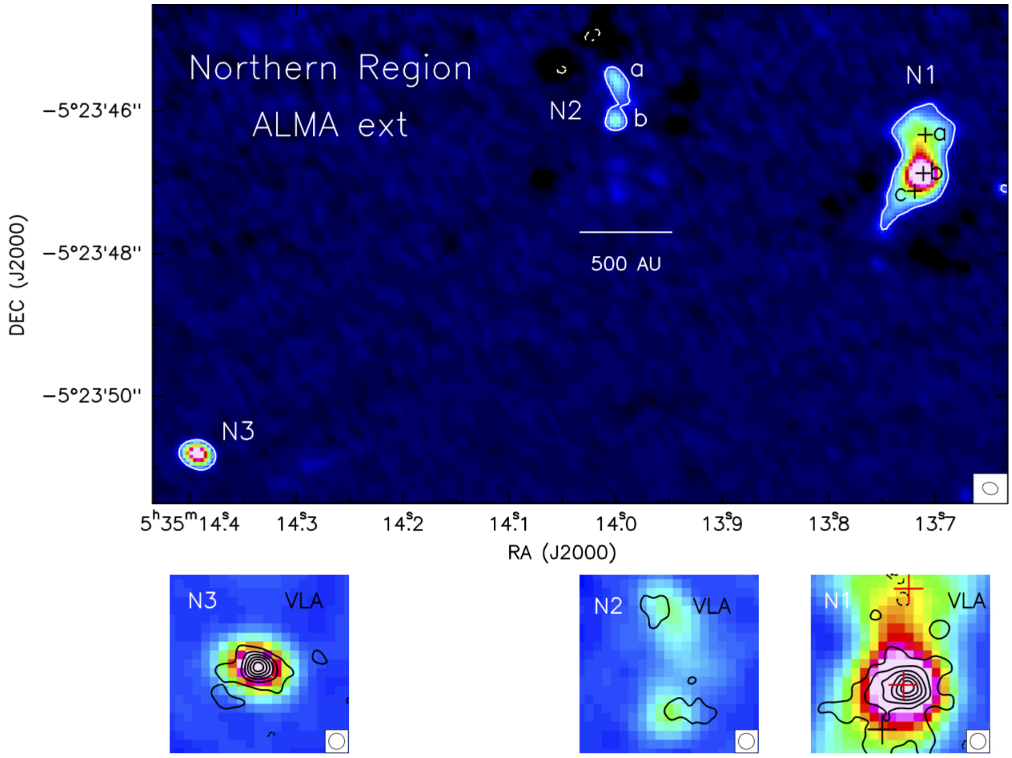

FIG. 2.— Top panel: ALMA 1.3 mm continuum emission towards the north of the OMC-1S region, using only the extended configuration. White (dashed) contours correspond to the 12σ (-12σ) emission. The ALMA beam is shown in the bottom-right corner. Lower panels: colorscale: idem as top panel; black contours: VLA 7 mm emission in a zoom of $1'' \times 1''$ centered on each source identified in the ALMA image. Contours are −2.5 (dashed), 2.5, 5, 7, 9, 11, 13, 15, and 17 times the rms of the image, 0.13 mJy beam^{-1}. In all the lower panels, the VLA beam is shown in the bottom-right corner. Plus signs in the top panel and in the bottom-right panel correspond to the peaks of the 3 Gaussians required to model the ALMA source N1.

The phase center for both observations was the same $\alpha(J2000) = 05^h\ 35^m\ 14\overset{s}{.}0$; $\delta(J2000) = -05^\circ\ 24'\ 00''$. The continuum image was obtained averaging line-free channels from four spectral windows (of 1.875 GHz width) centered at rest frequencies: 233.683 GHz, 231.323 GHz, 219.266 GHz, and 216.875 GHz, which covers a total bandwidth of 7.5 GHz.

The weather conditions were very good and stable with an average precipitable water vapor of 0.8 mm and an average system temperature of 60 K. The ALMA calibration included simultaneous observations of the 183 GHz water line with water vapor radiometers, used to reduce the atmospheric phase noise. Quasars J0541−0541, J0522−364, and J0750+1231 were used to calibrate the bandpass, the flux scale, the atmosphere and the gain fluctuations.

The data were calibrated, imaged, and analyzed using the Common Astronomy Software Applications (CASA). Imaging of the calibrated visibilities was done using the task CLEAN. We combined the two epochs with the task CONCAT in CASA. The resulting (dynamic-range limited) image rms noise was 0.7 mJy beam^{-1} at an angular resolution of $0\overset{''}{.}28 \times 0\overset{''}{.}22$ with PA = 81.64°. We also generated an image using only the extended configuration, in order to extract the compact sources. In this case, the rms of the 1.3 mm continuum is 0.45 mJy beam^{-1}, and the synthesized beam was $0\overset{''}{.}22 \times 0\overset{''}{.}17$, with PA=73.37°. Throughout the paper, we will refer to the rms noise of the extended configuration image by σ. We used the ROBUST parameter of CLEAN in CASA set to 0 for an optimal compromise between angular resolution and sensitivity. The millimeter continuum image obtained for OMC-1S was corrected by the primary beam attenuation. The primary beam at this wavelength had a full width at half maximum of about 27″.

2.2. *VLA at 7 mm*

The observations were made with the Very Large Array of NRAO[9] in the continuum mode at 7 mm (43.34 GHz) during 2004 November 10. The effective bandwidth of the observations was 100 MHz. At this epoch, the VLA was in A configuration, providing baselines covering projected lengths from 0.68 to 36 km (99–5200 kλ). This corresponds to a Largest Angular Scale to which the VLA was sensitive of 0.9″.

The phase center of the observations was $\alpha(J2000) = 05^h\ 35^m\ 14\overset{s}{.}0$; $\delta(J2000) = -05^\circ\ 24'\ 03''$, very close to the center of the radio cluster reported by Zapata et al. (2004). The absolute amplitude calibrator was J1331+ 305 (with an adopted flux density of 1.45 Jy) and the phase calibrator was J0541−056 (with a bootstrapped flux density of 1.10 ± 0.09).

The data were acquired and reduced using the recommended VLA procedures for high-frequency data, including the fast-switching mode with a cycle of 120 s. We used the ROBUST parameter of IMAGR in AIPS set to 0. The resulting image had an angular resolution of $0\overset{''}{.}065 \times 0\overset{''}{.}053$ with PA = −7.73°, but we smoothed the image to a final circular beam of 0.09″ in order to be more sensitive to faint and extended structure. The rms noise of the smoothed image is 0.13 mJy beam^{-1}. The 7 mm continuum image was also corrected by the primary beam attenuation. The primary beam

[9] The National Radio Astronomy Observatory is a facility of the National Science Foundation operated under cooperative agreement by Associated Universities, Inc.

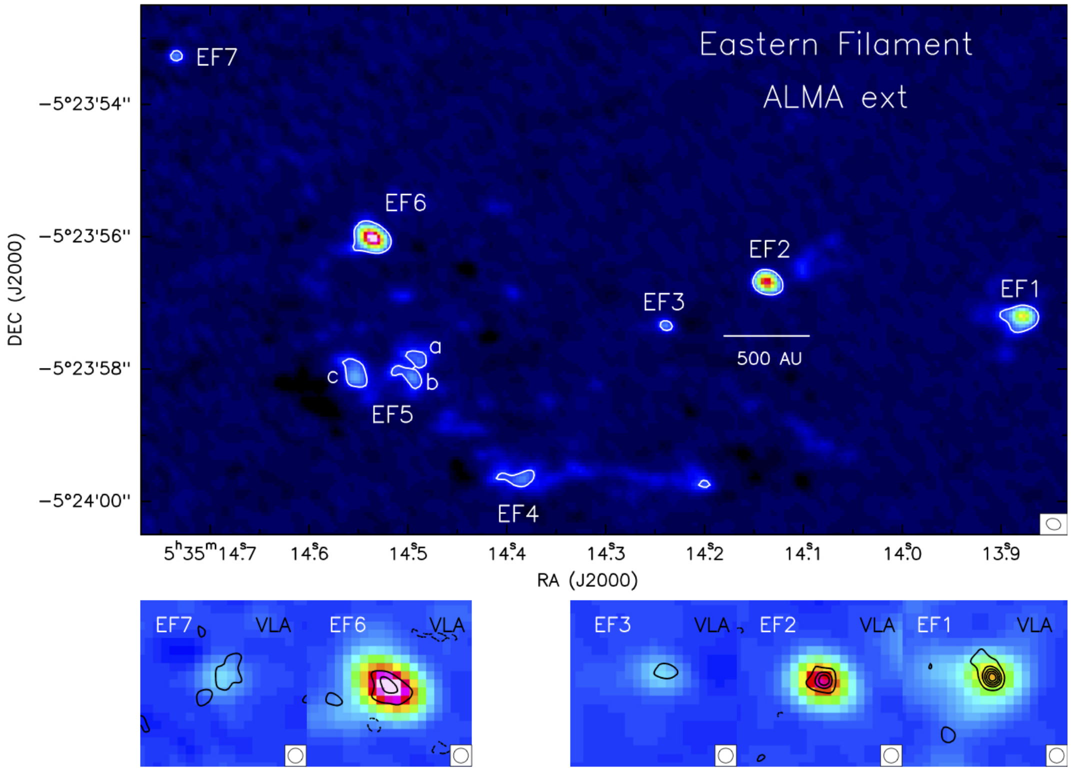

FIG. 3.— Same as Fig. 2 for the Eastern Filament of OMC-1S.

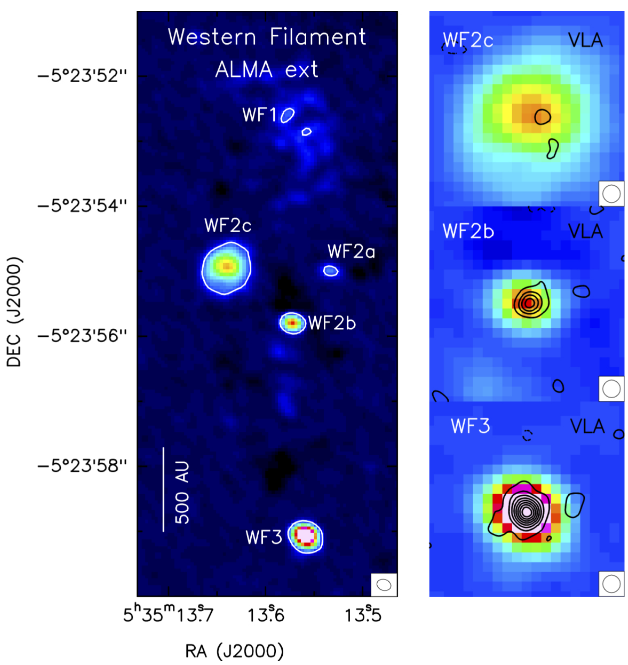

FIG. 4.— Same as Fig. 2 for the Western Filament of OMC-1S.

at this wavelength has a full width at half maximum of about 60″.

3. RESULTS

In Fig. 1 we present the ALMA 1.3 mm continuum emission towards OMC-1S with an angular resolution of $\sim 0.25''$, corresponding to $\sim$ 100 AU. The strongest millimeter sources detected by ALMA coincide very well with the sources already detected with the Submillimeter Array (see, e. g., Figure 1 of Zapata et al. 2005), but the ALMA image, about two orders of magnitude deeper, reveals additionally a number of faint point-like sources as well as a striking extended emission around the strong millimeter sources. We identify three main filamentary structures, plus three additional sources to the north of the image, which do not seem to belong to any filamentary structure. Two of the main filaments lie in the central part of the image, with the eastern one (hereafter, the 'Eastern Filament') elongated in the east-west direction, and the western one (the 'Western Filament') elongated in the north-south direction. The third filament, which is the most prominent one, lies about 10″ to the south (hereafter, the 'Southern Filament') and is also elongated in the east-west direction.

Embedded within the filamentary structures, we identify 14 strong millimeter sources or cores with peak intensity $> 40\sigma$, and these cores are separated approximately the same distance within the parent filament. In the Eastern Filament, the average separation between cores is $\sim$ 1920 AU; in the Western Filament, the separation between the two strongest cores is $\sim$ 1270 AU; and in the Southern Filament, the average separation is $\sim$ 1030 AU.

In order to extract the point and fainter sources detected by ALMA, we generated an image using only the extended configuration data. In Figs. 2, 3, 4 and 5 we show a zoom of the ALMA image of Fig. 1 on the four different regions/filaments identified in this figure. We identified 31 compact sources above a 12σ threshold (white contour in the figures; in this identification, we did not take into account those sources whose 12σ contour encompasses an area smaller than half of the beam). For the case of N1 and SF6, which are the

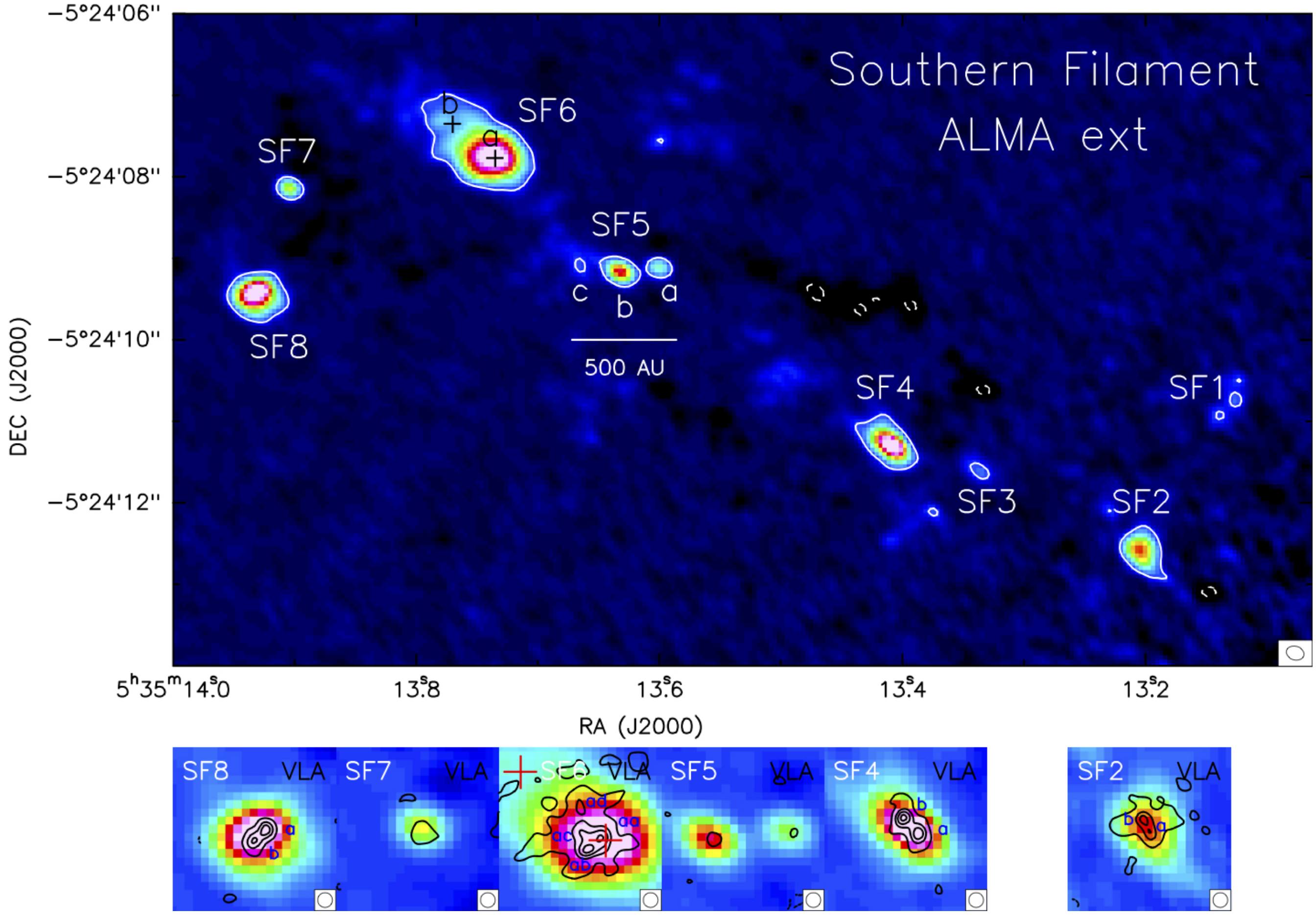

FIG. 5.— Same as Fig. 2 for the Southern Filament of OMC-1S. For the case of SF2, and SF6 we additionally show the contour at 6σ to make the structure clearer. Plus signs in the top panel and in the third lower panel correspond to the peaks of the 2 Gaussians required to model the ALMA source SF6.

strongest and most extended millimeter sources in the region, we identified subcomponents (using only the extended configuration data) by fitting 2D Gaussians and inspecting the residuals: if the residuals lie above the 12σ detection threshold, we required the inclusion of an additional Gaussian. Among the 31 identified sources, 11 sources belong to the Southern Filament (named SF1 to SF8, with SF5 consisting of 3 components and SF6 consisting of 2 components); 9 sources belong to the Eastern Filament (named EF1 to EF7, with EF5 consisting of 3 components), 6 sources belong to the northern region (N1 to N3, with N1 consisting of 3 components and N2 consisting of 2 components), and 5 sources belong to the Western Filament (named WF1 to WF3, with WF2 consisting of 3 components). The majority of the identified millimeter sources are either grouped within each core (i. e., at distances < 500 AU of the core peak, e. g., WF2, SF5) or lie at a distance consistent with the typical separation between cores in each filament (e. g., EF7, WF1). We note that the Eastern Filament seems to have two 'arms', the northern arm including EF1, EF2, EF3, EF6, and EF7, and the southern arm including EF4 and EF5. Since EF4 and EF5 are interconnected by extended emission which reaches the EF6 and EF2 sources (see Figs. 1 and 3), it seems reasonable to think that the two arms should have a common origin.

In Table 1 we give the position, peak intensity, flux density, deconvolved size and P.A. of the 31 identified millimeter sources, after performing 2D Gaussian fits using the extended+compact configuration image (Fig.1). In the table, we also provide an estimate of the mass of gas and dust for each millimeter source, using the flux density given in column (5) of Table 1, and assuming a dust temperature of 25 K, and a dust (+gas) mass opacity coefficient at 1.3 mm of 0.00899 cm^2 g^{-1} (Column 6 of Table 1 of Ossenkopf & Henning 1994, corresponding to agglomerated dust grains with thin ice mantles at densities 10^6 cm^{-3}). The dust temperature is estimated from observations of the NH_3(1,1) and (2,2) transitions by Wiseman & Ho (1998) of the Orion-KL and OMC-1S regions. These authors provide an image of the ratio of NH_3(2,2) to (1,1) integrated intensities, and for OMC-1S the ratio ranges from 0.5 to 1, corresponding to rotational temperatures from 18 to 33 K (for opacities of the NH_3(1,1) transition around 1, Table 2 of Wiseman & Ho 1998). Thus, we adopt an average temperature of 25 K for all the millimeter sources. Although some of the millimeter sources might be slightly more evolved than others (see Section 4) we adopt the same dust temperature because no big variations are expected given the embedded nature of the OMC-1S region (e. g., Sánchez-Monge et al. 2013). We estimated an uncertainty in the masses due to an uncertainty in the dust opacity of a factor of about two. The derived masses range from 0.02 to 1.5 $M_\odot$.

Using the 7 mm data from the VLA in its most extended

TABLE 1
PARAMETERS OF THE SOURCES DETECTED WITH ALMA AT 1.3 MM IN OMC-1S

Source	Position[a] α(J2000)	Position[a] δ(J2000)	$I_\nu^{1.3\mathrm{mm}\ a}$ (mJy beam^{-1})	$S_\nu^{1.3\mathrm{mm}\ a}$ (mJy)	Dec.size ($''\times''$)	Dec.PA (°)	Mass[b] ($M_\odot$)	Association[c]
N1a	05:35:13.709	−05.23.46.33	44 ± 2	293 ± 19	0.65 × 0.51	128	0.76	-
N1b	05:35:13.711	−05.23.46.87	118 ± 3	279 ± 10	0.30 × 0.26	7	0.73	137–347
N1c	05:35:13.719	−05.23.47.12	45 ± 2	419 ± 22	0.96 × 0.50	129	1.09	-
N2a	05:35:13.999	−05.23.45.63	30 ± 2	102 ± 9	0.62 × 0.16	20	0.27	-
N2b	05:35:13.998	−05.23.46.08	33 ± 2	97 ± 8	0.40 × 0.27	154	0.25	-
N3	05:35:14.392	−05.23.50.82	93 ± 1	114 ± 2	0.13 × 0.10	94	0.30	144–351
EF1	05:35:13.878	−05.23.57.21	35 ± 1	62 ± 2	0.27 × 0.15	109	0.16	139–357
EF2	05:35:14.135	−05.23.56.69	57 ± 1	76 ± 2	0.15 × 0.13	84	0.20	141–357
EF3	05:35:14.238	−05.23.57.38	8.4 ± 0.3	13.8 ± 0.8	0.22 × 0.17	102	0.04	-
EF4	05:35:14.386	−05.23.59.64	16 ± 1	197 ± 16	1.34 × 0.49	61	0.51	-
EF5a	05:35:14.497	−05.23.57.84	10 ± 1	48 ± 8	0.56 × 0.40	50	0.12	-
EF5b	05:35:14.510	−05.23.58.02	9 ± 2	24 ± 7	0.52 × 0.18	91	0.06	-
EF5c	05:35:14.552	−05.23.58.06	18 ± 1	176 ± 12	1.10 × 0.45	31	0.46	-
EF6	05:35:14.535	−05.23.56.02	84 ± 2	134 ± 5	0.22 × 0.16	53	0.35	145–356
EF7	05:35:14.734	−05.23.53.28	14.6 ± 0.6	15 ± 1	− × −	−	0.04	
WF1	05:35:13.578	−05.23.52.50	4.0 ± 0.6	19 ± 4	0.73 × 0.25	144	0.05	-
WF2a	05:35:13.531	−05.23.55.00	14.1 ± 0.8	25 ± 2	0.26 × 0.17	68	0.06	-
WF2b	05:35:13.571	−05.23.55.81	50 ± 1	65 ± 3	0.14 × 0.12	64	0.17	136–356
WF2c	05:35:13.638	−05.23.54.94	51 ± 2	236 ± 11	0.50 × 0.42	128	0.61	136–355
WF3	05:35:13.558	−05.23.59.08	134 ± 3	188 ± 6	0.17 × 0.13	31	0.49	136–359
SF1	05:35:13.125	−05.24.10.63	5.9 ± 0.8	9 ± 2	− × −	−	0.02	-
SF2	05:35:13.204	−05.24.12.57	72 ± 4	245 ± 16	0.47 × 0.28	13	0.64	132–413
SF3	05:35:13.339	−05.24.11.59	15 ± 1	56 ± 6	0.51 × 0.30	47	0.15	-
SF4	05:35:13.409	−05.24.11.27	106 ± 5	236 ± 17	0.36 × 0.18	48	0.61	134–411
SF5a	05:35:13.601	−05.24.09.13	30 ± 2	66 ± 5	0.42 × 0.14	92	0.17	-
SF5b	05:35:13.631	−05.24.09.17	56 ± 1	83 ± 3	0.20 × 0.14	82	0.22	-
SF5c	05:35:13.661	−05.24.09.03	7 ± 1	10 ± 2	0.27 × 0.09	63	0.03	-
SF6a	05:35:13.735	−05.24.07.77	111 ± 3	591 ± 20	0.58 × 0.44	74	1.54	137–408
SF6b	05:35:13.770	−05.24.07.35	23 ± 2	379 ± 38	0.98 × 0.92	143	0.98	-
SF7	05:35:13.903	−05.24.08.16	38 ± 1	49 ± 2	0.15 × 0.12	88	0.13	-
SF8	05:35:13.931	−05.24.09.45	116 ± 4	280 ± 12	0.32 × 0.25	111	0.73	139–409

[a] Position, intensity and flux density derived by fitting a 2D Gaussian using the image obtained after combining the extended+compact configurations. Uncertainty in the peak intensity and flux density is given by the fit. Point sources should have deconvolved sizes smaller than $0.10'' \times 0.05''$.

[b] Masses derived using the flux density given in column (5), and assuming a dust temperature of 25 K, and a dust (+gas) mass opacity coefficient at 1.3 mm of 0.00899 cm^2 g^{-1} (Ossenkopf & Henning 1994, see main text). The uncertainty in the masses due to the opacity law is estimated to be a factor of 2.

[c] Other names given in the literature (Smith et al. 2004; Zapata et al. 2005).

configuration, we can further study the substructure of the cores identified in the ALMA image, down to $0.09''$ or 40 AU. The small panels of Figs. 2, 3, 4 and 5 present a zoom of each ALMA core in colorscale, with the 7 mm continuum emission overplotted in black contours. We identified those 7 mm sources above the 5σ threshold. As can be seen in Fig. 2, the ALMA sources N3 and N1b have clear counterparts at 7 mm. In the Eastern Filament, sources EF1, EF2 and EF6 also have 7 mm counterparts (Fig. 3), similar to WF2b and WF3 in the Western Filament (Fig. 4). Finally, in the Southern Filament, SF2, SF4, SF6 and SF8 have 7 mm counterparts above the 5σ threshold (Fig. 5). After comparison of the 7 mm emission among the different regions/filaments, it is obvious that while the 7 mm counterparts in the northern region, Eastern Filament and Western filament are single sources, all the 7 mm counterparts of the ALMA sources in the Southern Filament harbor substructure, with the ALMA source being split into two components (SF2, SF4 and SF8) or even 4 components (SF6, where the 4 components show all emission above the 5σ threshold with a closed contour).

Table 2 summarizes the properties of the identified 7 mm sources: their peak position, peak intensity, and flux density (integrated inside the 2.5σ contour). In the Table, we also give the peak intensity of the 1.3 cm emission from Zapata et al. (2004). Using these values, and taking into account the positive spectral indices inferred by Zapata et al. (2004) for the 1.3 cm counterparts, a non-negligible part of the 7 mm emission could be contribution from emission at longer wavelengths. Therefore, we cannot disentangle with this information only whether the 7 mm emission comes mainly from free-free or thermal dust emission, and we refrain from estimating masses of gas and dust using the 7 mm emission.

TABLE 2
PARAMETERS OF THE SOURCES DETECTED WITH THE VLA AT 7 MM IN OMC-1S

Source	Position[a]		$I_\nu^{7\mathrm{mm}\ a}$	$S_\nu^{7\mathrm{mm}\ a}$	$I_\nu^{1.3\mathrm{cm}\ b}$
	α(J2000)	δ(J2000)	(mJy)	(mJy)	(mJy)
N1b	05:35:13.709	−05.23.46.88	1.91	17.2	0.59
N3	05:35:14.392	−05.23.50.82	1.88	5.19	0.78
EF1	05:35:13.876	−05.23.57.22	1.65	2.30	0.55
EF2	05:35:14.135	−05.23.56.68	1.14	1.49	0.85
EF6	05:35:14.536	−05.23.56.02	0.76	2.03	< 0.21
WF2b	05:35:13.571	−05.23.55.80	1.32	1.75	0.57
WF3	05:35:13.558	−05.23.59.07	2.47	5.37	1.00
SF2a	05:35:13.203	−05.24.12.62	0.80	4.06[c]	0.26
SF2b	05:35:13.206	−05.24.12.54	0.85		< 0.21
SF4a	05:35:13.405	−05.24.11.33	1.14	4.13[c]	0.78
SF4b	05:35:13.411	−05.24.11.23	1.27		0.78
SF6aa	05:35:13.737	−05.24.07.76	0.93	13.1[c]	0.15
SF6ab	05:35:13.742	−05.24.07.82	0.96		0.15
SF6ac	05:35:13.742	−05.24.07.76	0.84		< 0.21
SF6ad	05:35:13.746	−05.24.07.57	0.69		< 0.21
SF8a	05:35:13.928	−05.24.09.41	1.09	2.43[c]	0.42
SF8b	05:35:13.933	−05.24.09.47	0.96		0.42

[a] Position of the peak intensity, peak intensity and flux density integrated within the 2.5σ contour. Uncertainty in the peak intensity is the rms noise of the image, 0.13 mJy beam^{-1}. Units of the peak intensity are mJy beam^{-1}.

[b] Peak intensity at 1.3 cm from Zapata et al. (2004). For non-detections, an upper limit of 3σ is given. For SF4, SF6 and SF8 the position of the peak of the emission at 1.3 cm lies exactly in between the 7 mm positions of SF4a and SF4b, SF6a and SF6b, and SF8a and SF8b. Thus, we tentatively assigned half of the 1.3 cm peak intensity to each of these 7 mm sources.

[c] The flux density integrated within the 2.5σ contour includes both 'a' and 'b' sources for SF2, SF4, and SF8, and 'aa', 'ab', 'ac' and 'ad' sources for SF6.

4. ANALYSIS

4.1. *Fragmentation level vs evolutionary stage and density*

As seen in the previous section, the ALMA and VLA observations have revealed the structure of the millimeter emission in OMC-1S, at spatial scales spanning almost two orders of magnitude, from 2200 AU (corresponding to the Largest Angular Scale of the ALMA data) down to ~ 40 AU (corresponding to the angular resolution of the VLA data). This allowed us to identify three extended filamentary structures, with 14 strong millimeter sources or cores embedded in them (Section 3), as well as further substructure within these cores. Given that the typical separation between cores in the filaments ranges from 1000 to 2000 AU (Section 3), we will consider any emission/structure within radii of ~ 500 AU from the peak of each core as emission belonging to that core. We note that the VLA 7 mm 5σ detections correspond to a 1.3 mm threshold of 40σ, assuming a spectral index of 2. Thus, our VLA+ALMA dataset allows us to study the fragmentation properties down to spatial resolutions of ~ 40 AU for mass sensitivities of ~ 0.05 $M_\odot$ (estimated using a flux density of 40σ or 18 mJy at 1.3 mm and the same assumptions of Table 1).

In the following, we define the 'fragmentation level' of each core as the number of closed contours above the detection threshold at each wavelength (12σ at 1.3 mm, and 5σ at 7 mm), within a region of 1000 AU of diameter. This is similar to the definition used in Palau et al. (2013, 2014, 2015), but in these works the fragmentation was assessed within a region of 0.1 pc, while in the present work we assess the fragmentation in a region about one order of magnitude smaller. In the case of no closed contours but the single Gaussian fit clearly requiring an additional Gaussian (see Section 3), we counted each Gaussian as a separate source (this is the case of N1 and SF6 in the ALMA data). In all cases, the core peak identified in ALMA data has a clear 7 mm counterpart, and these have been counted as one single source. In Table 3, we list the 14 ALMA cores and their fragmentation level within 1000 AU. From that table, it is obvious that most of the cores in the Southern Filament present a fragmentation level higher than most of the cores in the Eastern Filament. The Western Filament is an intermediate case.

In order to search for the physical processes yielding the high fragmentation level in the Southern Filament, we explored first the possibility that this is an evolutionary effect. For this, the most appropriate method would be to build the Spectral Energy Distribution (SED) for each core. However, to do this we would need mid-infrared and far-infrared information for each core at an angular resolution better than ~ 2″, and this is not available for the ALMA cores in OMC-1S. We crossed our list of cores with the Orion *Spitzer* and *Herschel* catalogs of Megeath et al. (2012) and Furlan et al. (2016), and only found identified *Spitzer*/IRAC point sources corresponding to N3 and WF2b, and no sources in *Spitzer*/MIPS or *Herschel*/PACS catalogs. The sources N3 and WF2b are also detected in the mid-infrared observations of Smith et al. (2004), together with EF6 and WF3. With a total of 4 cores with mid-infrared detections, it is definitely not possible to study any trend of fragmentation with SED properties. Instead, we have collected data for all the cores at different wavelengths, so that we may have a rough idea of the possible evolutionary stage of each core.

On one hand, in Fig. 6 we present a CAHA K_s image of the OMC-1S region. To obtain this near-infrared image, we used the Calar Alto Public Archive[10] and download a set of near-infrared images taken between 2011 December 13 and 15, with the OMEGA-2000 Camera on the 3.5m telescope at Calar Alto Observatory. We processed the raw images along with a set of proper calibration files using our reduction pipelines[11], in a sequence similar to that described by Román-Zúñiga et al. (2015). As can be seen in the figure, some of the ALMA cores (overplotted in blue contours) are detected in the infrared, and these are mainly located in the Western and Eastern Filaments. In addition, we searched for *Chandra* X-ray counterparts to the ALMA cores (Rivilla et al. 2013). Finally, we also studied the 1.3 cm emission associated with the cores, following Zapata et al. (2004), together with their respective spectral indices. We summarize all these properties in Table 3 and Fig. 6.

After compiling all these data for the ALMA cores, we tentatively assigned an evolutionary stage for each core. We as-

[10] http://www.caha.es/caha-public-archives.html

[11] In a nutshell, our pipelines consist of IRAF and Fortran routines that provided a two-pass sky subtraction reduction, centroid corrected dither registering, a < 0.2″ rms astrometric solution, as well as aperture and PSF photometry catalogs for all detectable sources.

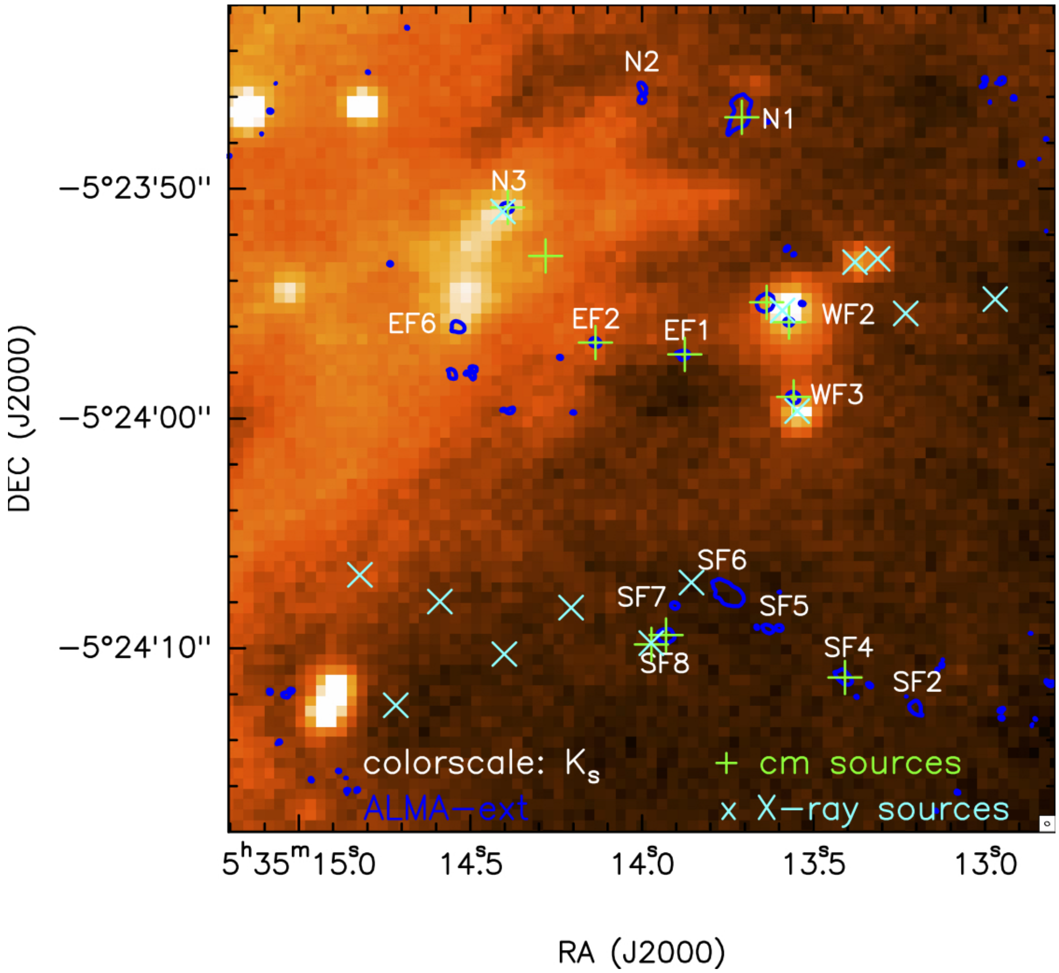

FIG. 6.— Colorscale: CAHA K_s band. Blue contours: ALMA 1.3 mm continuum emission using only the extended configuration. Contours correspond to the 12 times the rms noise of the map, 0.45 mJy beam^{-1}. The 14 identified ALMA cores, where we have studied fragmentation, are labeled in white, and the beam of the ALMA image is shown in the bottom right corner. Green plus signs: 1.3 cm sources from Zapata et al. (2004); Turquoise crosses: X-ray sources from Rivilla et al. (2013).

signed the stage of Class 0/I for the most embedded sources, and Class I/II for the more evolved objects probably having only a faint envelope. Intermediate cases would be assigned the Class I stage. We based our classification on the following criteria: i) near-infrared emission and X-ray emission are usually associated with young stellar objects dominated by a disk (no envelope, e. g., Rivilla et al. 2013; Povich et al. 2016), and detection in at least one of these signposts, and association with HH objects (no molecular outflows) would suggest a Class I/II nature; ii) if a source is detected in all the signposts of Table 3, with the outflow being molecular, we consider it to be in an intermediate stage (i. e., Class I); iii) sources driving molecular outflows (traced by SiO, CO, or water masers) and being associated with thermal centimeter emission ($\alpha^{3.6-1.3\mathrm{cm}} > 0$), with no detection in the infrared or X-rays are typically deeply embedded sources (e. g., Liu et al. 2014, Pech et al. 2016), suggesting a Class 0/I nature; iv) if a source has not been detected in any of the signposts listed in Table 3, we consider it as deeply embedded (i. e., Class 0/I), since the extreme compact nature of the dust emission suggests that an hydrostatic core is already formed.

In Fig. 7 we plot the fragmentation level against this tentative evolutionary stage. Although the statistics used to build Fig. 7 are extremely poor (essentially because most of the sources seem to be in the Class 0/I stage), there would seem to be a possible trend of decreasing fragmentation with evolutionary stage, which should be confirmed by including more sources in the later stages.

Even though Fig. 7-top would suggest a decreasing trend of fragmentation level with evolutionary stage, it is true that in the earliest stage there are a wide spread of fragmentation levels: from the lowest possible (around 1 source) up to the highest (5 sources). An ingredient which could be playing a role in the early fragmentation of the cores is their density structure. This was studied by Palau et al. (2014), who find that the fragmentation level in a sample of massive dense cores of $\gtrsim 0.1$ pc seems to be tightly related to the density of the core within the diameter of 0.1 pc, which in turn depends on the density profile and the central density of the core. With this in mind, we used an approximate method to test in our data the effect of the density structure of the core, assuming that the temperature structure does not change significantly from one core to the other and thus that the differences in the intensity profiles mainly reflect the differences in density profiles. For each core, we estimated the mass (following the same assumptions of Section 3) enclosed within a given diameter, which we take to be 1000 AU, and then converted this into density. By doing this, if the density profile is rather flat

TABLE 3
SUMMARY OF PROPERTIES OF THE CORES EMBEDDED OMC-1S

Core	N_{mm} [a]	Separation [b] (AU)	IR? [c]	X-rays? [c]	Outf? [c]	HMC? [c]	cm? [c]	$\alpha^{3.6-1.3cm}$ [c]	Tentative Class [c]	n_{1000AU} [d] ($\times 10^7$ cm^{-3})
N1	3	190	N	N	SiO	Y	Y	$> 1.6 \pm 0.3$	0/I	11
N2	2	190	N	N	N	N	N	–	0/I	5.5
N3	1	–	Y	Y	HH	N	Y	$> 1.9 \pm 0.3$	I/II	0.7
EF1	1	–	N	N	SiO?	Y	Y	$> 1.4 \pm 0.3$	0/I	0.7
EF2	1	–	N	N	SiO?	Y	Y	1.1 ± 0.1	0/I	1.6
EF6	1	–	Y	N	OOS	N	N	–	I/II	3.7
WF2[e]	3	390–500	Y	Y	SiO	Y	Y	$> 1.1 \pm 0.3$	I	6.8
WF3	1	–	Y	Y	CO	Y	Y	$> 1.8 \pm 0.3$	I	4.0
SF2	2	40	N	N	N	N	N	–	0/I	8.0
SF4	3	60–430	N	N	mas	Y	Y	1.9 ± 0.1	0/I	8.6
SF5	3	170–210	N	N	N	Y	N	–	0/I	7.2
SF6	5	40–270	N	N	SiO	N	N	–	0/I	12
SF7	1	–	N	N	N	N	N	–	0/I	2.1
SF8	2	50	N	Y	mas	Y	Y	$> 1.9 \pm 0.2$	0/I	5.8

[a] Number of millimeter sources within 1000 AU including both ALMA and VLA data. For the case of SF4, N_{mm} includes SF4a, SF4b, and SF3.

[b] Range of separations between the sources within the core.

[c] References for infrared emission (IR): Smith et al. (2004) and this work; X-ray emission: Rivilla et al. (2013); Outflows (Outf): in case of outflow detection, we give the outflow tracer: CO (Zapata et al. 2005), SiO (Zapata et al. 2006), HH (Herbig-Haro object, Smith et al. 2004), OOS: region from which at least six HH objects originate, with coordinates (J2000): R.A. 05h35m14.56s, Dec. −05 : 23 : 54, with a position error of $\pm 1.5''$, O'Dell & Doi 2003), mas: water masers from Zapata et al. (2007); Hot Molecular Core (HMC): Zapata et al. (2007) and Palau et al., in prep.; 1.3 cm centimeter emission (cm): Zapata et al. (2004). $\alpha^{3.6-1.3cm}$, the spectral index between 3.6 and 1.3 cm, is taken from Zapata et al. (2004). The Tentative Class assigned to each core has been estimated from a global assessment of the previous properties (see Section 4).

[d] Density of H_2 molecules within 1000 AU (of diameter), obtained after measuring the flux density in a region of 1000 AU of diameter ($\sim 2.5''$), and converting this into a mass, adopting the same assumptions as in Table 1.

[e] For the case of core WF2, we give the properties associated with the strongest millimeter source, WF2b, but note that WF2c is also associated with centimeter emission, with $\alpha^{3.6-1.3cm} > 0.8 \pm 0.3$. Regarding the hot molecular core, this is associated with WF2c.

we will obtain a high mass within the given diameter, while if the density profile is highly concentrated, the mass within the same diameter will be smaller (assuming similar central densities). In Fig. 7-bottom we plot the fragmentation level against the density within 1000 AU. The figure shows that the higher the density, the higher the fragmentation level[12]. Actually, the average density within 1000 AU for the fragmenting cores is 8.1×10^7 cm^{-3}, while the average density within 1000 AU for the non-fragmenting cores is about a factor of 4 smaller, 2.1×10^7 cm^{-3}.

4.2. *Typical separations between the fragments*

In order to analyze the typical separations between the fragments, we calculated the mean surface density of companions (MSDC), Σ_θ, for all the 31 fragments listed in Table 1. The MSDC has been widely used to investigate the transition from pairs to groups in distinct scenarios that include young star clusters and dense cores (Gómez et al. 1993; Bate et al. 1998; Kraus & Hillenbrand 2008; Román-Zúñiga et al. 2010, Tafalla & Hacar 2015). Following the prescription by Simon (1997), we estimated the angular separations, θ from each to every other fragment in the list using the RA, DEC coordinates and grouped them in 0.2 dex annuli within $-6 < \log\theta < 0$. Then, Σ_θ is computed as the number of elements in each annulus, $N_p(\theta)$, divided by the area, normalized by the total number of elements. The MSDC is equivalent this way, to the two-point correlation function (TPCF), W_θ, that compares the value of Σ_θ with a uniform, random distribution of points in an area of the same size as our field ($A_m = 10^{-4}$ deg ^{2}). If N_r is the number of the randomly distributed points that fall in each of our annuli, then $W_\theta = (N_p/N_r) - 1$. To determine N_r, we averaged the output from 5×10^4 drawings using a simple Monte Carlo routine. Then,

$$\Sigma_\theta(\mathrm{TPCF}) = (N_p/A_m)(1 + W_\theta),$$

can be compared directly to the value of Σ_θ estimated from direct counting in the anular bins.

The results of this calculation are shown in Fig. 8. The figure shows that Σ_θ is anticorrelated to θ from $-4.5 < \log\theta < -3.4$ (about 44 to 556 AU), then the distribution appears to flatten out to $\log\theta \approx -3$ (about 1397 AU), followed by another short fall and a bump from −3 to −2.7 and from −2.7 to −2.5, respectively. The values of the MSDC and the TPCF are very consistent down to this last value, but above it, the function shows an abrupt decrease, indicating where the angular separation reaches the field size. Two aspects are remarkable:

[12] We would like to emphasize that the density averaged over all the core is not correlated with the fragmentation level because this average density is not taking into account the density distribution. What is well correlated with the fragmentation level is the density averaged at a given radius, which takes into account the central density and the density profile of the core.

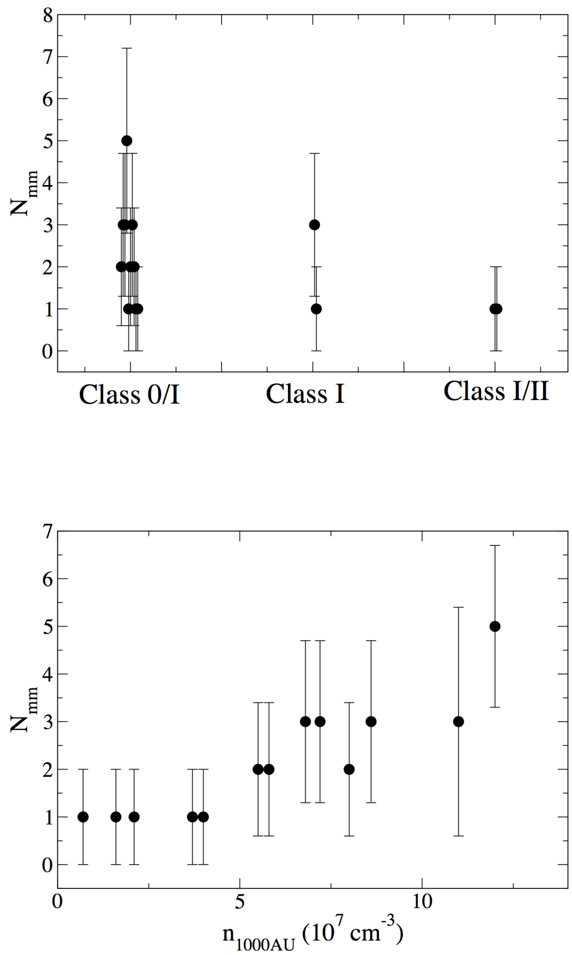

FIG. 7.— *Top:* Fragmentation level vs tentative evolutionary class. *Bottom:* Fragmentation level vs density (of H_2 molecules) enclosed within 1000 AU.

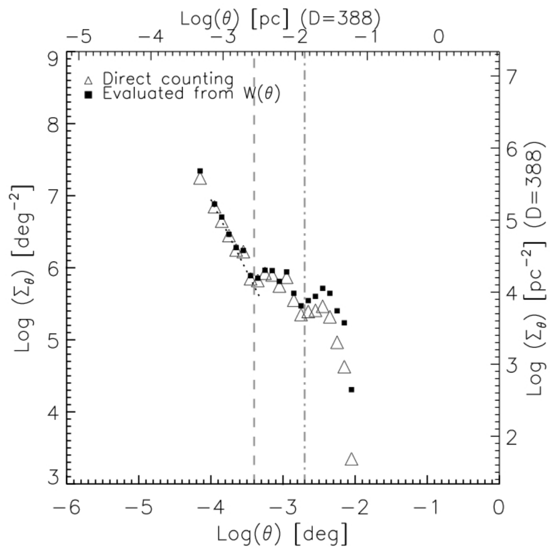

FIG. 8.— Mean surface density of companions vs angular separation. White triangles and black squares correspond to the 'direct counting' and '$W(\theta)$' (or two-point correlation function) methods, respectively (Section 4.2).

one is that the limits of the two observed breaks in the plot at $\log\theta = -3.4$ and -2.7 (556 and 2787 AU respectively) correspond very well to the limits at which we notice breaks in the fragmentation scales of our data (Section 3 and Table 3). Second, the linear fit in the $-4.5 < \log\theta < -3.4$ range has a well defined slope of -1.05 suggesting uniform separation behavior of fragments across the region within that range of scales. Moreover, the linear fit and the slope near 1 are similar to values obtained by Hartmann (2002) and Kraus & Hillenbrand (2008) for the MSDC of single stars in Taurus over a similar range of scales.

5. DISCUSSION

In the previous section we studied the fragmentation level of the OMC-1S cores detected with ALMA, and showed that most of the cores of the Southern Filament present a high fragmentation level compared to the cores of the other filaments. We studied whether this could be related to the evolutionary stage of the cores and found hints of a possible trend of decreasing fragmentation with the evolutionary stage (Fig. 7-top), although we definitely need to improve the statistics. This is consistent with the observed trend of multiplicity fraction[13] decreasing with evolutionary stage, from Class 0 to Class I, reported by several authors such as Connelley et al. (2008), Chen et al. (2013), Duchene & Kraus (2013), and Tobin et al. (2016). Such a trend is expected if fragmentation takes place bound to the gas potential and the potential is dominated by one central object, naturally leading to the decrease of distances between the fragments (e. g., Sadavoy & Stahler 2017). It is also expected from dynamical evolution, since three-body interactions tend to destroy wide binary systems (e. g., Kroupa et al. 1999; Kaczmarek, Olczak, & Pfalzner 2011; Duchene & Kraus 2013; Li et al. 2016).

Thus, the trend of fragmentation/multiplicity decreasing with age seems to be confirmed with the most recent works, both observational and theoretical. However, it still remains to be understood which process sets the pristine fragmentation level of a core. OMC-1S is an excellent region to study this because of the high number of detected cores with ALMA, and because most of these cores seem to harbor young stellar objects at very early evolutionary stages (Table 3).

There are several processes that have been proposed in the literature to play a role in setting the pristine fragmentation of a core. First, the magnetic field should inhibit fragmentation (e. g., Boss et al. 2004; Vázquez-Semadeni et al. 2005; Hennebelle et al. 2011, Commerçon et al. 2011; Fontani et al. 2016). However, the observational works which have

[13] At the small spatial scales where we have studied fragmentation (~ 500 AU of radius), one could already refer to the detected sources within the cores as forming a 'multiple system'. However, from our data alone it is not possible to assure the protostellar nature of all the detected millimeter sources, and it is neither possible to study whether the sources near the core peaks are gravitationally bound to them or not. For this reasons, we refrain from calling our study a 'multiplicity study' but rather prefer to call it a 'fragmentation study'.

measured the magnetic field strength in regions with different fragmentation levels have drawn no clear conclusions (e. g., Busquet et al. 2016). Further submillimeter polarization observations of OMC-1S with higher angular resolution than the current ones (Matthews et al. 2009) would be extremely useful to study the effect of the magnetic field in the fragmentation of the cores in this region.

Second, 'turbulent support' has been proposed also in the literature as providing support against gravity and yielding to a few massive fragments (Zhang et al. 2009, 2015; Wang et al. 2011, 2014; Pillai et al. 2011, Lu et al. 2015). However, this is an oversimplified treatment of the true nature of turbulence, as it is difficult to think that the complex, non-linear and anisotropic motions generated by turbulence might combine to precisely provide support against gravity for a given core, as argued by some authors (e. g., Dobbs et al. 2005; Ballesteros-Paredes et al. 2011). Furthermore, observational studies that have measured the magnitude of the non-thermal motions show that they are too weak to explain the observed masses (e. g., Csengeri et al. 2011).

Third, rotational fragmentation could potentially be an important agent to determine the fragmentation level of a core, as this would be an efficient way of removing angular momentum as the core is collapsing (e. g., Arreaga-Garcia 2017 and references therein). This has been proposed, for example, for the formation of the L1551NE binary (Lim et al. 2016). In OMC-1S, we would need to detect a high number of ALMA cores in molecular gas tracers in order to study the role of rotation of the core on its fragmentation, but such a dataset is not currently available for this region.

Recently, Palau et al. (2014, 2015) have studied the aforementioned processes in a sample of 19 massive dense cores and found that the fragmentation level within cores of 0.1 pc is best correlated with the density structure of the cores, rather than with the non-thermal velocity dispersion (Palau et al. 2015) or even the rotational-to-gravitational energy (Palau et al. 2014). Interestingly, Lee et al. (2015) also find no clear correlation of the fragmentation level with non-thermal velocity dispersion or rotational-to-gravitational energy in L1448N, but a good correlation of higher fragmentation with density. Other recent observational works supporting the crucial role of the density on the star formation history of the cores are those of Samal et al. (2015), Sharma et al. (2016), and Figueira et al. (2017). All these works favor pure thermal Jeans fragmentation, as in this case, the higher the density of the core, the smaller the Jeans mass and thus the higher number of fragments is expected. In the previous section we have studied this in OMC-1S, and find again an increasing trend of higher fragmentation with density within 1000 AU, very consistent with the previous works but now at scales about one order of magnitude smaller.

If Jeans fragmentation is at work, we should find masses of the sources comparable to the Jeans mass, and separations comparable to the Jeans length. If we take an average density within 1000 AU for the fragmenting cores of about $\sim 8 \times 10^7$ cm^{-3} (Section 4.1), and a temperature of 25 K, the Jeans mass is $\sim$ 0.09 $M_\odot$, while the Jeans length is 770 AU (following Bontemps et al. 2010, Palau et al. 2015). For our ALMA data, the mass sensitivity is 0.018 $M_\odot$ (for the 12σ detection threshold), fully sensitive to the Jeans mass, and for the VLA data the mass sensitivity is $\sim$ 0.2 $M_\odot$ (for the 5σ detection threshold and in the case of thermal dust emission). Similarly, the Jeans length is fully resolved by our ALMA (and VLA) data ($\lesssim$ 100 AU). Among the 31 sources detected with ALMA, 18 have masses below 0.3 $M_\odot$ (Table 1), only a factor of 3 larger than the Jeans mass. And we should still keep in mind that the masses reported in Table 1 should be an upper limit to the true mass of the source because we have calculated the masses using the flux density, and thus including extended emission around the sources, which implies in most cases a factor of 3–10 larger flux density.

Regarding the Jeans length, in Table 3 we provide the range of separations between the fragments embedded in the ALMA cores, which range from 40 AU up to 500 AU. The separation of $\sim$ 500 AU, which is comparable to the Jeans length, is also coincident with a break found in the MSDC curve presented in Section 4.2 and Fig. 8. As shown in Fig. 8, the MSDC increases with a power law of index $\sim$ -1 for separations $<$ 500 AU, which is consistent with ordered fragmentation at scales smaller than the Jeans length. In addition, the Jeans length for a density of 10^7 cm^{-3} is $\sim$ 2000 AU, consistent with the average separations between cores in the main filaments (Section 3), and comparable to the separation for which a second break on the MSDC curve is found in Fig. 8.

This suggests two level Jeans-like fragmentation, as found by Teixeira et al. (2016) in the Orion Molecular Cloud 1 northern filament. These authors study the role of turbulence and magnetic field and find that they cannot explain the observed Jeans lengths, and suggest that thermal Jeans fragmentation is taking place simultaneously with the local collapse of the clumps, which would naturally reduce the separations, as expected also from simulations of collapsing filaments (e.g., Pon et al. 2011). This is fully consistent with our results and the recent detection of large-scale collapse in OMC-1S (Hacar et al. 2017a).

We would like to remark however that, although it seems that the fragmentation properties in OMC-1S can be explained through pure thermal Jeans fragmentation, a recent work studying multiplicity in the Perseus cloud finds that systems with separations of around $\lesssim$ 200 AU should have formed through disk fragmentation, while systems with separations $\gtrsim$ 1000 AU should have formed through thermal fragmentation (e. g., Tobin et al. 2016). However, this behavior seems to be different from the Taurus cloud (Kraus et al. 2011), and should not necessary apply to Orion. For the case of Orion, fragmentation has been studied on spatial scales larger than 1000 AU and does not cover the 'disk fragmentation' domain (e. g., Kainulainen et al. 2016b), preventing from drawing conclusions regarding this model. Thus the mechanism of formation of the closest systems in OMC-1S (such as SF2, SF6, SF8) should be studied in more detail in order to test the disk fragmentation scenario for these cases.

Finally, a note regarding nomenclature. There is currently some confusion in the literature with the nomenclature used to describe the fragmentation processes, especially those including the role of turbulence. For example, some authors call 'turbulent fragmentation' to the process yielding fragments with masses larger than the thermal Jeans mass, i. e., the Jeans masses are estimated using the Jeans criterion but replacing the factor related to temperature by a factor related to the non-thermal line width (equations 2, 4 and 5 of Palau et al. 2015). This approach presents some limitations, in particular the non-thermal line width could be due to processes different from internal turbulence (e. g., infall). The data presented in this work can be reproduced without this turbulent support and thus there is no need to invoke turbulent support at these small ($\sim$ 1000 AU) scales. There are also a number of authors who refer to 'gravoturbulent fragmentation' to the fragmentation taking place in a self-gravitating turbulent medium, where the density is determined by the enhancements created by turbulence (e. g., Padoan & Nordlund 2002; Schmeja et al. 2004; Fisher 2004; Goodwin et al. 2004; Hennebelle & Chabrier 2008, Offner et al. 2010; Kirk et al. 2017). In this scenario, the Jeans mass estimation is reduced to a pure thermal Jeans mass at the scales we consider in this study. Our data are thus fully consistent with this gravoturbulent fragmentation, what we call here 'pure thermal Jeans fragmentation'.

6. CONCLUSIONS

With the aim of studying the fragmentation properties down to spatial scales of multiple systems, we conducted 1.3 mm ALMA observations towards OMC-1S, with an angular resolution of $\sim 0.2''$, corresponding to spatial scales of ~ 100 AU, and a sensitivity 2 orders of magnitude better than previous works. In addition, these observations have been complemented with 7 mm VLA observations at $\sim 0.1''$ of angular resolution. Our main conclusions can be summarized as follows:

- The deep 1.3 mm ALMA continuum image reveals 3 filamentary structures in OMC-1S (the Eastern, Western and Southern Filaments), with 14 cores (millimeter sources above 40σ) embedded in them, whose typical separations are ~ 1500 AU. In total, 31 millimeter continuum sources (above a 12σ threshold) have been identified, most of them embedded within the cores of the filaments and only four do not belong to any filamentary structure.

- 7 mm emission is detected towards almost all the ALMA cores, revealing further substructure down to 40 AU. This is particularly important in the Southern Filament, where almost all the ALMA cores split up into several sources.

- By compiling near-infrared, X-ray, centimeter, and outflow information for all the ALMA cores, a tentative evolutionary stage is assigned to each core. We found a possible trend of fragmentation level decreasing with evolutionary stage.

- Typical separations between the fragments are $\lesssim 560$ and ~ 2900 AU, indicative of a two-level fragmentation process.

- There is a correlation of fragmentation level with the density of the core within 1000 AU, as found in previous works studying fragmentation at one order of magnitude larger spatial scales, suggesting that fragmentation at the earliest stages and within spatial scales of ~ 1000 AU is following a thermal Jeans process.

In summary, considering that the fragmentation level within 1000 AU can be regarded as a first approach to the multiplicity of the core, the deep ALMA data presented here, together with the VLA data, seem to suggest that multiple systems with separations > 40 AU are formed through the same mechanisms that govern the fragmentation process at larger scales. This result deserves further investigation in order to disentangle the role of disk fragmentation in the formation of multiple systems in OMC-1S, something which definitely requires kinematic information from molecular gas tracers.

A.P. is grateful to Eric Keto for thoughtful discussions, and to Víctor Rivilla for sharing the X-ray source catalog. A.P. acknowledges financial support from UNAM-DGAPA-PAPIIT IA102815 grant, México. L.Z. acknowledges financial support from DGAPA, UNAM, and CONACyT, México. R.E. acknowledges support by the Spanish MINECO grant AYA2014-57369-C3 (cofunded with FEDER funds) and MDM-2014-0369 of ICCUB (Unidad de Excelencia 'María de Maeztu'). G.B. acknowledges the support of the Spanish Ministerio de Economía y Competitividad (MINECO) under the grant FPDI-2013-18204. R.E., G.B., and J.M.G. are supported by the Spanish MICINN grant AYA2014-57369-C3. A.F. thanks the Spanish MINECO for funding support from grant AYA2016-75066-C2-2-P and ERC under ERC-2013-SyG, G. A. 610256 NANOCOSMOS. This paper makes use of the following ALMA data: ADS/JAO.ALMA#2015.1.00865.S. ALMA is a partnership of ESO (representing its member states), NSF (USA) and NINS (Japan), together with NRC (Canada), NSC and ASIAA (Taiwan), and KASI (Republic of Korea), in cooperation with the Republic of Chile. The Joint ALMA Observatory is operated by ESO, AUI/NRAO and NAOJ. This research has made use of the VizieR catalogue access tool, CDS, Strasbourg, France. The original description of the VizieR service was published in A&AS 143, 23. The authors made use of the GILDAS software (`http://www.iram.fr/IRAMFR/GILDAS`) and acknowledge the efforts of the GILDAS team to keep it up to date.

REFERENCES

Arreaga-García, G. 2017, Ap&SS, 362, #47
Ballesteros-Paredes, J., Hartmann, L. W., Vázquez-Semadeni, E., Heitsch, F., & Zamora-Avilés, M. A. 2011, MNRAS, 411, 65
Bate, M. R., Clarke, C. J., & McCaughrean, M. J. 1998, MNRAS, 297, 1163
Bontemps, S., Motte, F., Csengeri, T., & Schneider, N. 2010, A&A, 524, A18
Boss, A. P. 2004, MNRAS, 350, L57
Busquet, G., Estalella, R., Palau, A., et al. 2016, ApJ, 819, 139
Chabrier, G., Johansen, A., Janson, M., & Rafikov, R. 2014, Protostars and Planets VI, 619
Chen, X., Arce, H. G., Dunham, M. M., & Zhang, Q. 2012, ApJ, 747, L43
Chen, X., Arce, H. G., Zhang, Q., et al. 2013, ApJ, 768, 110
Chini, R., Hoffmeister, V. H., Nasseri, A., Stahl, O., & Zinnecker, H. 2012, MNRAS, 424, 1925
Commerçon, B., Hennebelle, P., & Henning, T. 2011, ApJ, 742, L9
Connelley, M. S., Reipurth, B., Tokunaga, A. T. 2008, AJ, 135, 2496
Csengeri, T., Bontemps, S., Schneider, N., Motte, F., & Dib, S. 2011, A&A, 527, A135
Csengeri, T., Bontemps, S., Wyrowski, F., et al. 2017, arXiv:1703.03273
Dobbs, C. L., Bonnell, I. A., & Clark, P. C. 2005, MNRAS, 360, 2
Duarte-Cabral, A., Bontemps, S., Motte, F., et al. 2013, A&A, 558, A125
Duchêne, G., & Kraus, A. 2013, ARA&A, 51, 269
Figueira, M., Zavagno, A., Deharveng, L., et al. 2016, arXiv:1612.08862
Fisher, R. T. 2004, ApJ, 600, 769
Fontani, F., Commerçon, B., Giannetti, A., et al. 2016, A&A, 593, L14
Furlan, E., Fischer, W. J., Ali, B., et al. 2016, ApJS, 224, 5
Gómez, M., Hartmann, L., Kenyon, S. J., & Hewett, R. 1993, AJ, 105, 1927
Gong, M., & Ostriker, E. C. 2015, ApJ, 806, 31
Goodwin, S. P., Whitworth, A. P., & Ward-Thompson, D. 2004, A&A, 423, 169
Guszejnov, D., Hopkins, P. F., & Ma, X. 2017, arXiv:1702.04431
Hacar, A., Alves, J., Tafalla, M., & Goicoechea, J. R. 2017a, arXiv:1703.03464
Hacar, A., Tafalla, M., & Alves, J. 2017b, arXiv:1703.07029
Hartmann, L. 2002, ApJ, 578, 914
Hennebelle, P., Commerçon, B., Joos, M., et al. 2011, A&A, 528, A72
Hennebelle, P., & Chabrier, G. 2008, ApJ, 684, 395-410
Henney, W. J., O'Dell, C. R., Zapata, L. A., et al. 2007, AJ, 133, 2192
Henshaw, J. D., Jiménez-Serra, I., Longmore, S. N., et al. 2017, MNRAS, 464, L31
Hopkins, P. F. 2013, MNRAS, 430, 1653
Johnstone, D., & Bally, J. 1999, ApJ, 510, L49
Kaczmarek, T., Olczak, C., & Pfalzner, S. 2011, A&A, 528, A144

Kainulainen, J., Hacar, A., Alves, J., et al. 2016a, A&A, 586, A27
Kainulainen, J., Stutz, A. M., Stanke, T., et al. 2016, arXiv:1603.05688
Kirk, H., Dunham, M. M., Di Francesco, J., et al. 2017, arXiv:1703.00506
Kounkel, M., Hartmann, L., Loinard, L., et al. 2017, ApJ, 834, 142
Kratter, K. M., & Matzner, C. D. 2006, MNRAS, 373, 1563
Kraus, A. L., & Hillenbrand, L. A. 2008, ApJ, 686, L111
Kraus, A. L., Ireland, M. J., Martinache, F., & Hillenbrand, L. A. 2011, ApJ, 731, 8
Kraus, S., Kluska, J., Kreplin, A., et al. 2017, ApJ, 835, L5
Kroupa, P., Petr, M. G., & McCaughrean, M. J. 1999, New Astronomy, 4, 495
Lee, K. I., Dunham, M. M., Myers, P. C., et al. 2015, ApJ, 814, 114
Li, Y., Kouwenhoven, M. B. N., Stamatellos, D., & Goodwin, S. P. 2016, ApJ, 831, 166
Lim, J., Hanawa, T., Yeung, P. K. H., et al. 2016, ApJ, 831, 90
Liu, H. B., Galván-Madrid, R., Forbrich, J., et al. 2014, ApJ, 780, 155
Lu, X., Zhang, Q., Wang, K., & Gu, Q. 2015, ApJ, 805, 171
Matthews, B. C., McPhee, C. A., Fissel, L. M., & Curran, R. L. 2009, ApJS, 182, 143
Megeath, S. T., Gutermuth, R., Muzerolle, J., et al. 2012, AJ, 144, 192
O'Dell, C. R., & Doi, T. 2003, AJ, 125, 277
Offner, S. S. R., Kratter, K. M., Matzner, C. D., Krumholz, M. R., & Klein, R. I. 2010, ApJ, 725, 1485
Ossenkopf, V., & Henning, T. 1994, A&A, 291, 943
Padoan, P., & Nordlund, Å. 2002, ApJ, 576, 870
Palau, A., Sánchez-Monge, Á., Busquet, G., et al. 2010, A&A, 510, A5
Palau, A., Fuente, A., Girart, J. M., et al. 2013, ApJ, 762, 120
Palau, A., Estalella, R., Girart, J. M., et al. 2014, ApJ, 785, 42
Palau, A., Ballesteros-Paredes, J., Vázquez-Semadeni, E., et al. 2015, MNRAS, 453, 3785
Pech, G., Loinard, L., Dzib, S. A., et al. 2016, ApJ, 818, 116
Pillai, T., Kauffmann, J., Wyrowski, F., et al. 2011, A&A, 530, A118
Pon, A., Johnstone, D., & Heitsch, F. 2011, ApJ, 740, 88
Povich, M. S., Townsley, L. K., Robitaille, T. P., et al. 2016, ApJ, 825, 125
Rivilla, V. M., Martín-Pintado, J., Sanz-Forcada, J., Jiménez-Serra, I., & Rodríguez-Franco, A. 2013, MNRAS, 434, 2313
Román-Zúñiga, C. G., Lada, C. J., & Alves, J. F. 2009, ApJ, 704, 183
Román-Zúñiga, C. G., Alves, J. F., Lada, C. J., & Lombardi, M. 2010, ApJ, 725, 2232
Román-Zúñiga, C. G., Ybarra, J. E., Megías, G. D., et al. 2015, AJ, 150, 80
Sadavoy S. I, Stahler S. W., 2017, arXiv, arXiv:1705.00049
Samal, M. R., Ojha, D. K., Jose, J., et al. 2015, A&A, 581, A5
Sánchez-Monge, Á., Palau, A., Fontani, F., et al. 2013, MNRAS, 432, 3288
Schmeja, S., & Klessen, R. S. 2004, A&A, 419, 405
Sharma, S., Pandey, A. K., Borissova, J., et al. 2016, AJ, 151, 126
Simon, M. 1997, ApJ, 482, L81
Smith, N., Bally, J., Shuping, R. Y., Morris, M., & Hayward, T. L. 2004, ApJ, 610, L117
Tafalla, M., & Hacar, A. 2015, A&A, 574, A104
Tahani, K., Plume, R., Bergin, E. A., et al. 2016, ApJ, 832, 12
Takahashi, S., Ho, P. T. P., Teixeira, P. S., Zapata, L. A., & Su, Y.-N. 2013, ApJ, 763, 57
Teixeira, P. S., Takahashi, S., Zapata, L. A., & Ho, P. T. P. 2016, A&A, 587, A47
Tobin, J. J., Looney, L. W., Li, Z.-Y., et al. 2016, ApJ, 818, 73
Vázquez-Semadeni, E., Kim, J., & Ballesteros-Paredes, J. 2005, ApJ, 630, L49
Walker-Smith, S. L., Richer, J. S., Buckle, J. V., et al. 2013, MNRAS, 429, 3252
Wang, K., Zhang, Q., Wu, Y., & Zhang, H. 2011, ApJ, 735, 64
Wang, K., Zhang, Q., Testi, L., et al. 2014, MNRAS, 439, 3275
Wiseman, J. J., & Ho, P. T. P. 1998, ApJ, 502, 676
Zapata, L. A., Rodríguez, L. F., Kurtz, S. E., O'Dell, C. R., & Ho, P. T. P. 2004, ApJ, 610, L121
Zapata, L. A., Rodríguez, L. F., Ho, P. T. P., et al. 2005, ApJ, 630, L85
Zapata, L. A., Ho, P. T. P., Rodríguez, L. F., et al. 2006, ApJ, 653, 398
Zapata, L. A., Ho, P. T. P., Rodríguez, L. F., Schilke, P., & Kurtz, S. 2007, A&A, 471, L59
Zhang, Q., Wang, Y., Pillai, T., & Rathborne, J. 2009, ApJ, 696, 268
Zhang, Q., Wang, K., Lu, X., & Jiménez-Serra, I. 2015, ApJ, 804, 141